Electronic Supplementary Material (ESI) for Journal of Materials Chemistry A.

Supporting Information

A High-Capacity Aqueous Zinc-Ion Battery Fiber with Air-Recharging Capability

Meng Liao, Jiawei Wang, Lei Ye, Hao Sun, Pengzhou Li, Chuang Wang, Chengqiang Tang, Xiangran Cheng, Bingjie Wang, and Huisheng Peng**

State Key Laboratory of Molecular Engineering of Polymers, Department of Macromolecular Science, and Laboratory of Advanced Materials, Fudan University, Shanghai, 200438, China.

* E-mail: wangbingjie@fudan.edu.cn; penghs@fudan.edu.cn

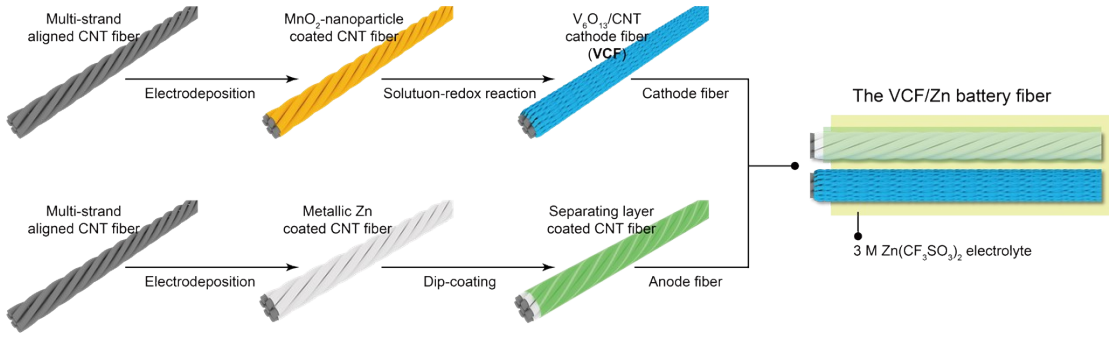

Figure S1. Schematic illustration of the preparation procedures of the VCF (V_6O_{13}/CNT cathode fiber) and the VCF/Zn battery fiber. Related detailed description is provided in Experimental section and **Note S1**.

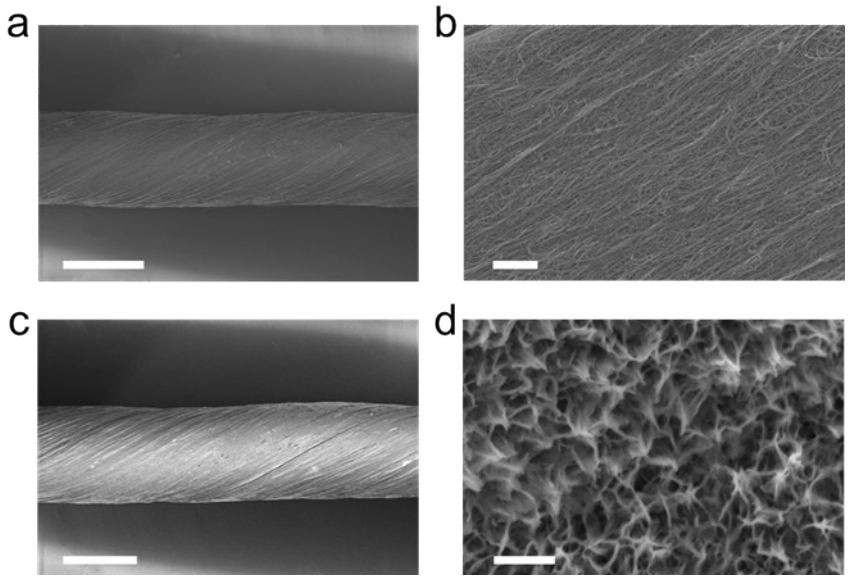

Figure S2. (a) and **(b)** SEM images of the multi-strand aligned CNT fiber. **(c)** and **(d)** SEM images of the MnO_2-nanoflower-coated CNT fiber. Scale bars, 200 μm in **(a)** and **(c)**, 2 μm in **(b)**, and 200 nm in **(d)**.

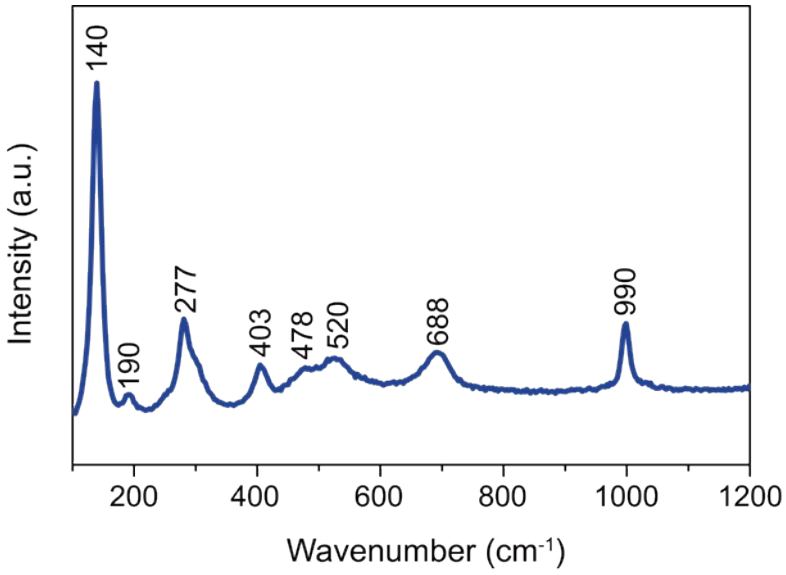

Figure S3. Raman spectrum of the VCF.

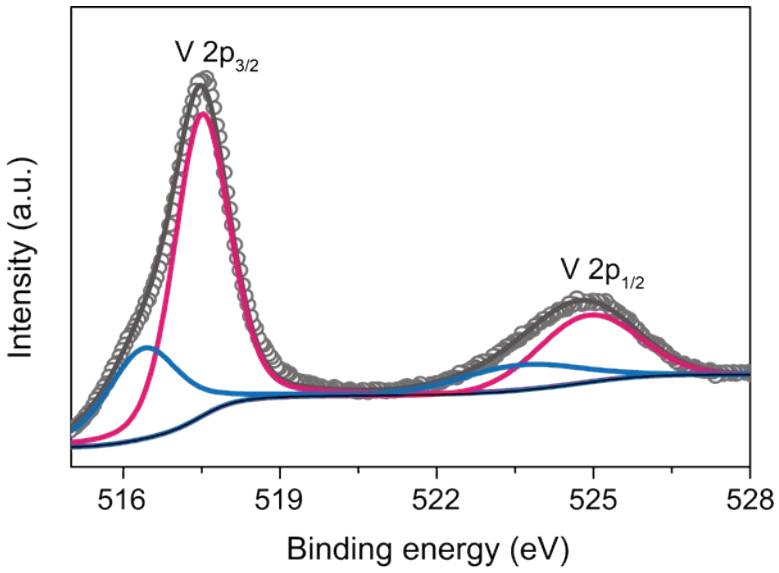

Figure S4. X-ray photoelectron spectroscopy with the V 2p spectra of the as-prepared VCF. Corresponding discussion is provided in **Note S3**.

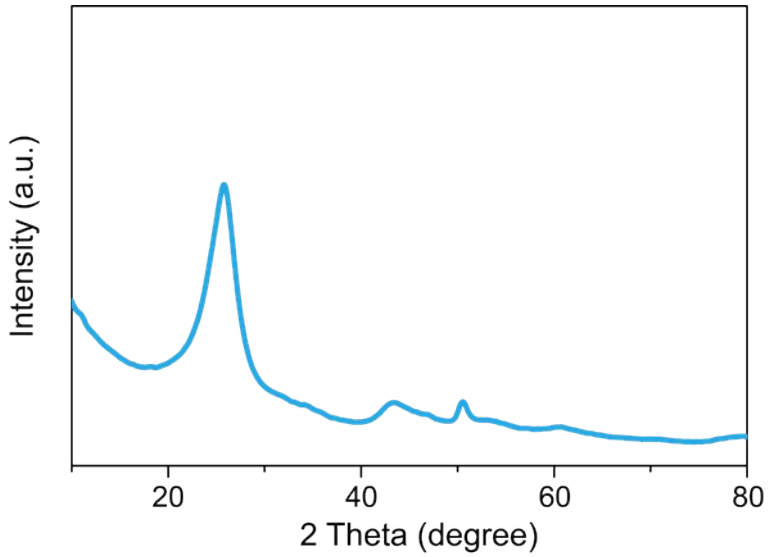

Figure S5. X-ray diffraction pattern of the as-fabricated VCF.

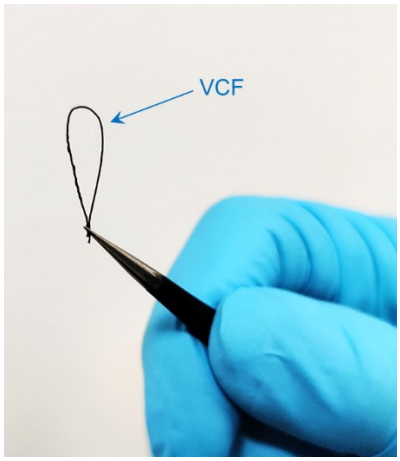

Figure S6. Photograph of a curved VCF.

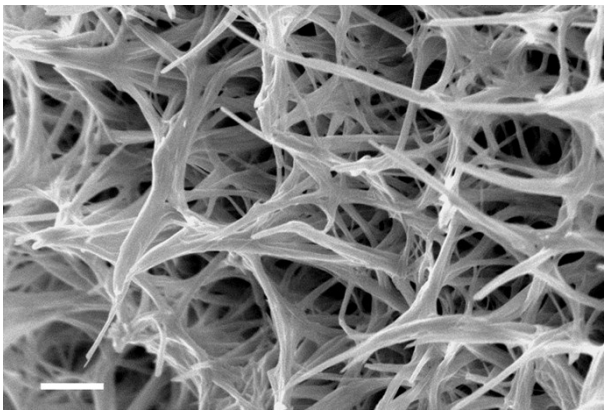

Figure S7. Interconnected V_6O_{13} nano-belts forming a 3D nest-like structure in the VCFs. Scale bar, 200 nm.

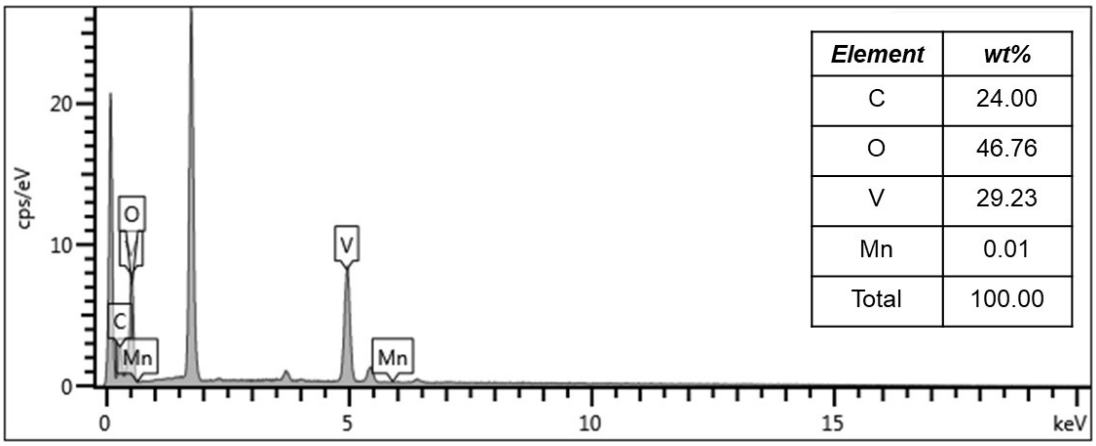

Figure S8. Element compositions of the as-prepared, free-standing VCF from scanning electron microscopy-element dispersive spectrometer analysis.

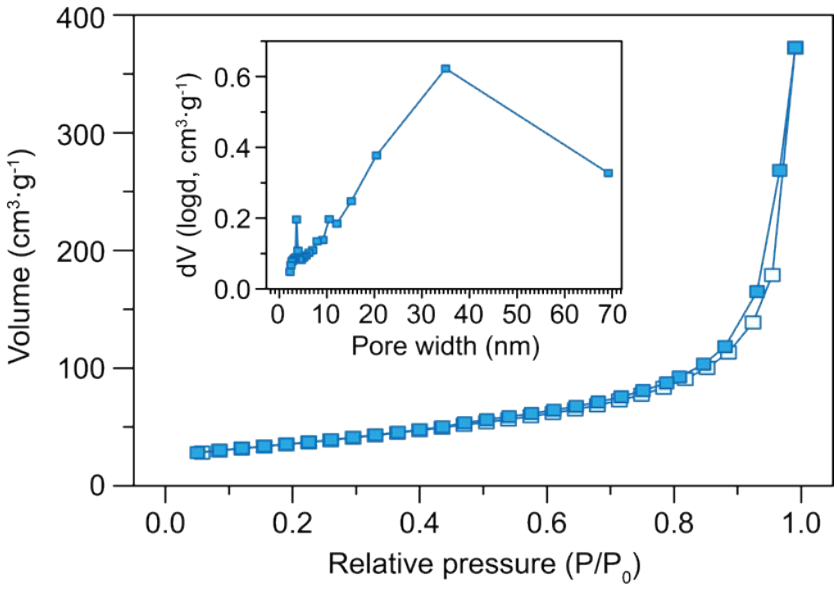

Figure S9. Nitrogen adsorption-desorption isotherm of the VCF (inset, the corresponding pore size distribution of the VCF). The specific surface area of the VCF was 171.3 $m^2 \cdot g^{-1}$.

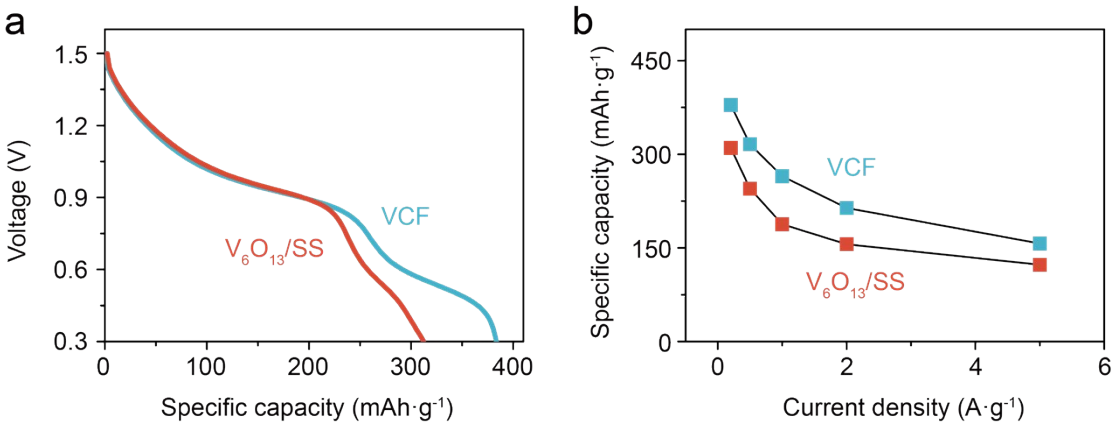

Figure S10. (a) Comparison of galvanostatic discharge curves of fiber batteries based on VCF (V_6O_{13}/CNT) and V_6O_{13}/SS (stainless steel yarn) at 200 mA·g^{-1}. **(b)** Specific capacity and capacity retention of the VCF and V_6O_{13}/SS fiber electrodes as a function of current density obtained from the galvanostatic discharge profiles. The use of aligned CNT fibers with high specific surface area contributed to the improved cathode utilization in VCFs.

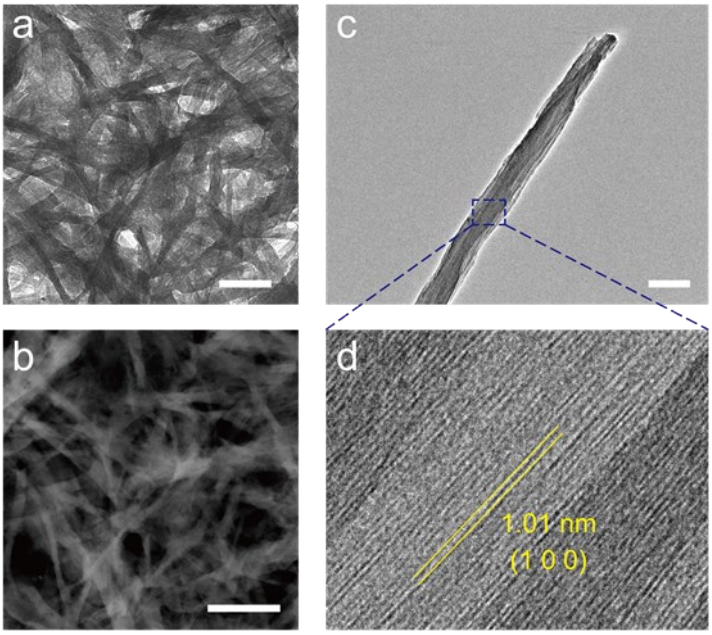

Figure S11. (a) and **(b)** Bright and dark-field transmission electron microscopy images of the VCF, respectively. **(c)** and **(d)** Transmission electron microscopy and high-resolution transmission electron microscopy images of a typical VCF, respectively. Scale bars, 200 nm in **(a)-(c)**.

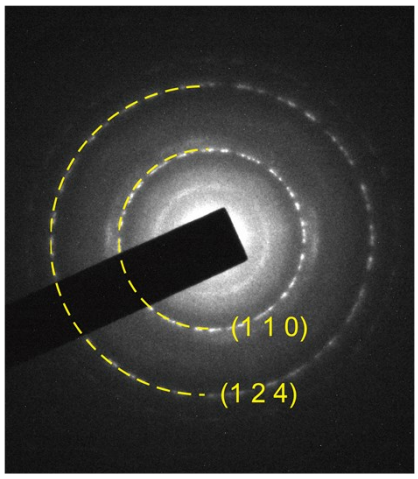

Figure S12. Selected area electron diffraction pattern of the VCF.

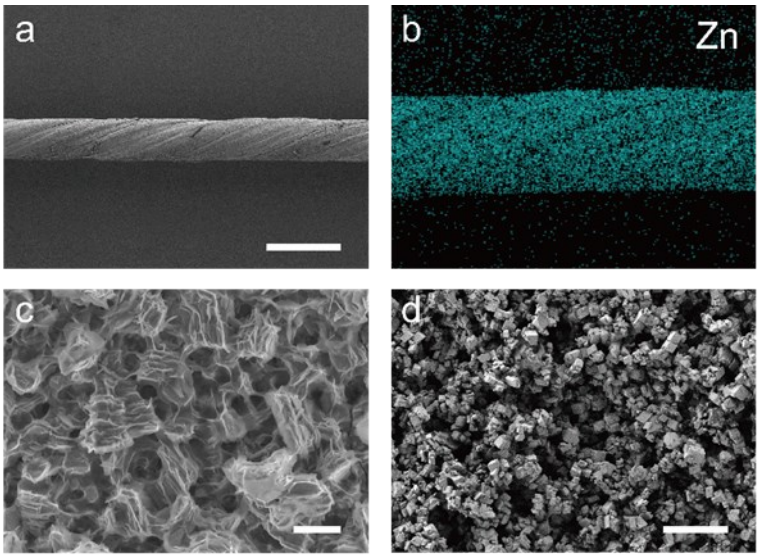

Figure S13. (a) Scanning electron microscopy image of the Zn-coated CNT anode fiber. **(b)** Elemental distribution of the Zn-coated anode fiber. **(c)** Surface morphology of the Zn-coated fiber. **(d)** Surface morphology of the Zn-coated fiber after the incorporation of a separating layer composed of porous $CaCO_3$. Scale bars, 200 μm in **(a)**, 2 μm in **(b)** and 20 μm in **(c)**.

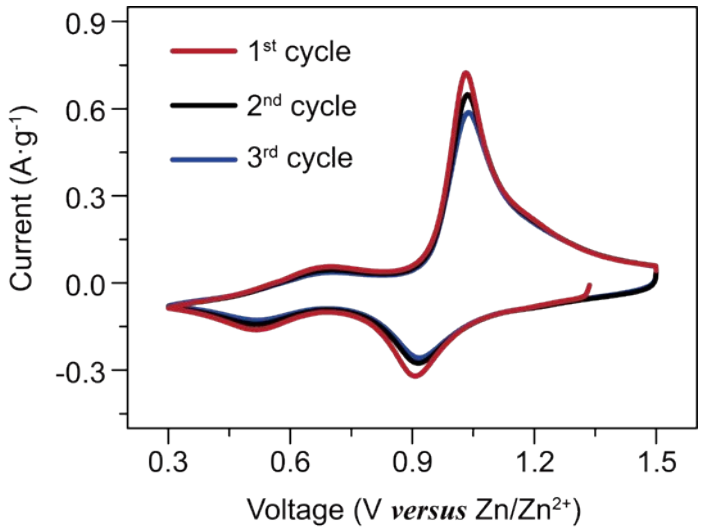

Figure S14. Cyclic voltammograms of the first three cycles of the VCF/Zn battery fiber at 0.2 $mV \cdot s^{-1}$.

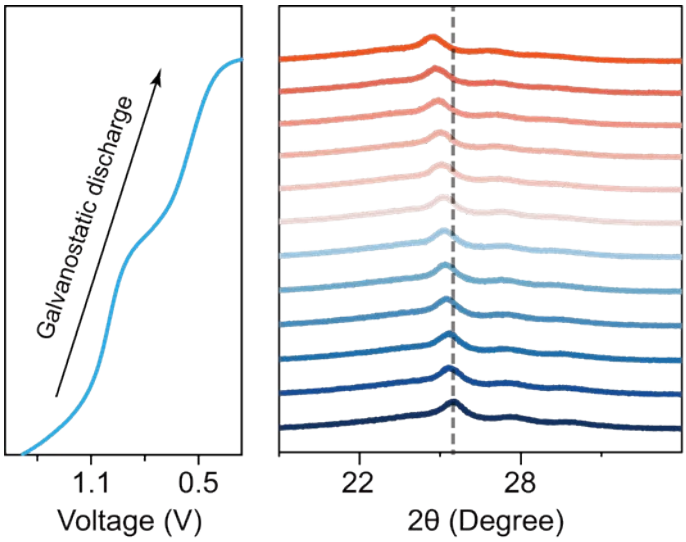

Figure S15. *In-situ* X-ray diffraction measurements of the VCF during the first galvanostatic discharge process.

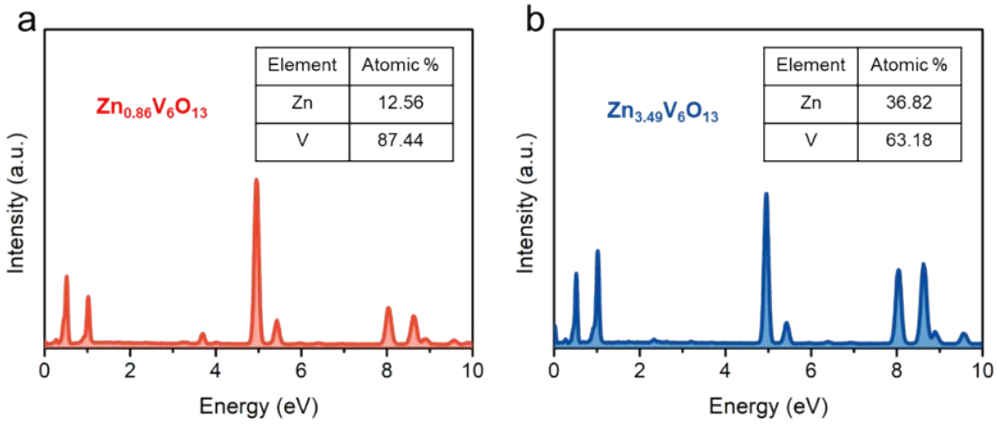

Figure S16. (a) Transmission electron microscopy-energy dispersive spectrometer analysis of the fully charged VCF and the quantification of elemental ratio. **(b)** Transmission electron microscopy-energy dispersive spectrometer analysis of the fully discharged VCF and the quantification of elemental ratio. Insets of **(a)** and **(b)** are the corresponding transmission electron microscopy images. Corresponding discussion is provided in **Note S3**.

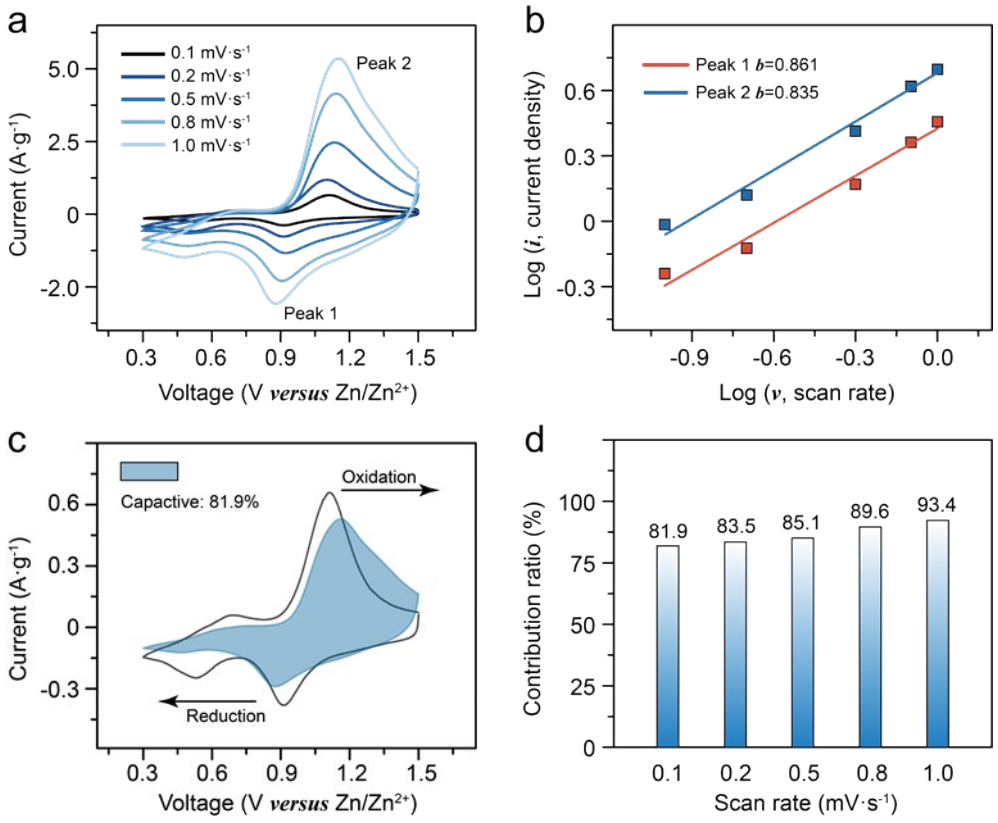

Figure S17. (a) Cyclic voltammograms of the VCF/Zn battery fiber at scan rate ranging from 0.1 to 1.0 mV·s^{-1}. **(b)** Plots of log(***i***) versus log(***v***) of the cathodic current response at the typical two peaks of the VCF labeled in **(a)**. The slopes of the fitted lines determine the *b* values. **(c)** Cyclic voltammogram displaying the capacitive contribution (light blue region) to the total current at 0.1 mV·s^{-1} of the VCF. **(d)** Percentages of capacity contributions of the VCF at increasing scan rates. Corresponding discussion is provided in **Note S2**.

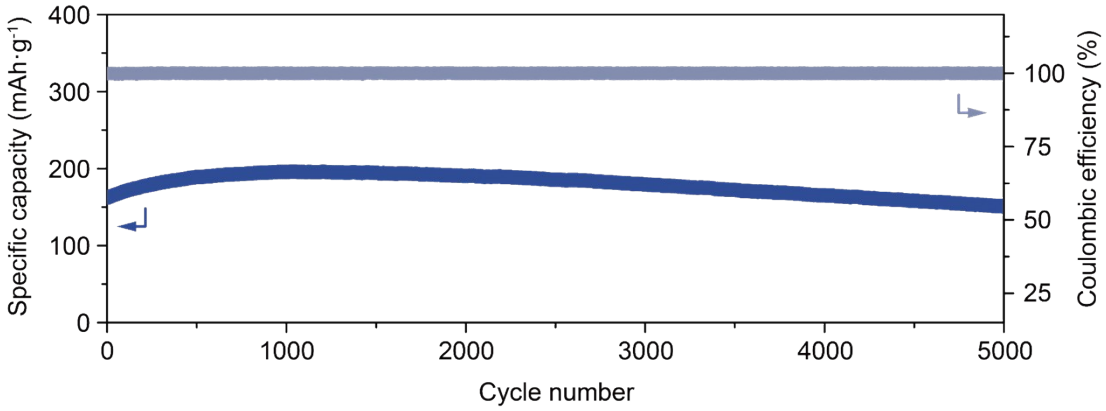

Figure S18. Cycling performance of the VCF in terms of specific capacity (deep blue) and the corresponding Coulombic efficiency (pale blue) at current density of 5 $A \cdot g^{-1}$.

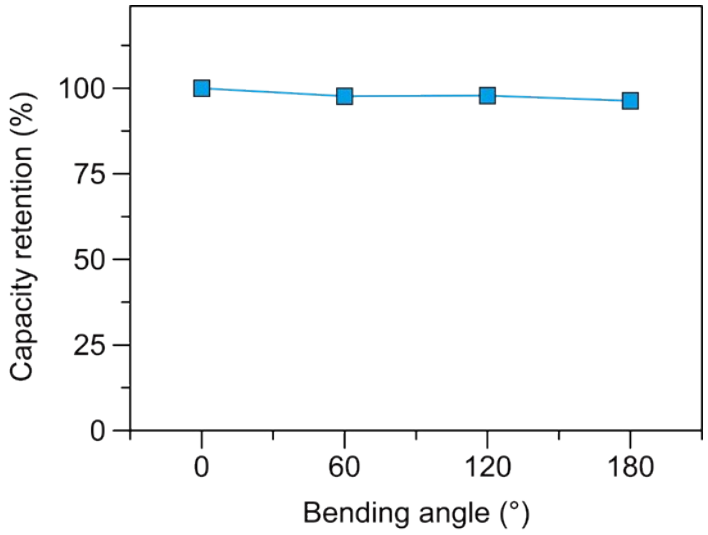

Figure S19. Dependence of the capacity retention on bending angle of the VCF/Zn battery fiber.

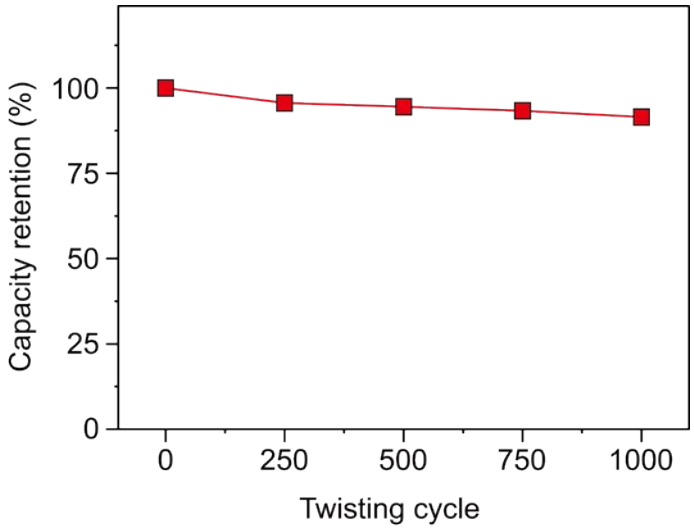

Figure S20. Dependence of the capacity retention on twisting cycle of the VCF/Zn battery fiber.

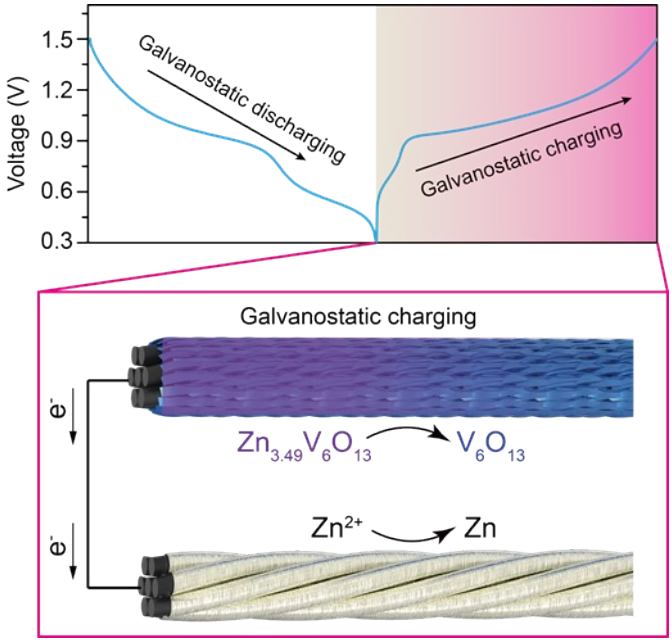

Figure S21. Typical profile and the corresponding schematic illustration of the galvanostatic charging process of the VCF/Zn battery fiber.

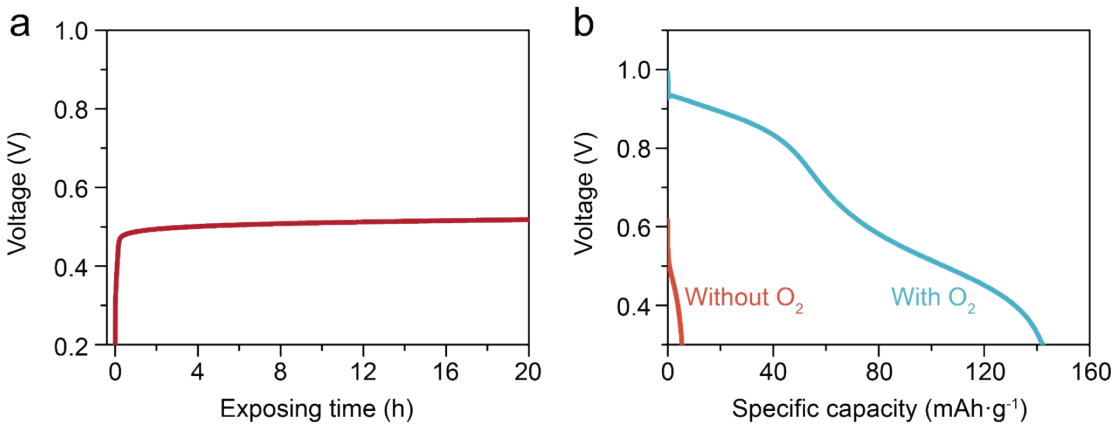

Figure S22. (a) Voltage-time curve of discharged VCF/Zn battery immersed in N_2-saturated aqueous $Zn(CF_3SO_3)_2$ electrolyte, where most of the O_2 was removed. The immediate increase of open-circuit voltage could be attributed to the concentration polarization on the surface of discharged VCF. The ultimate voltage under O_2-eliminated was below 0.6 V, which was much lower than that of in ambient air (~1.1 V). **(b)** Galvanostatic discharge curves at 100 mA·g^{-1} of VCFs after 20 h of exposing time with and without O_2. Corresponding discussion is provided in **Note S3**.

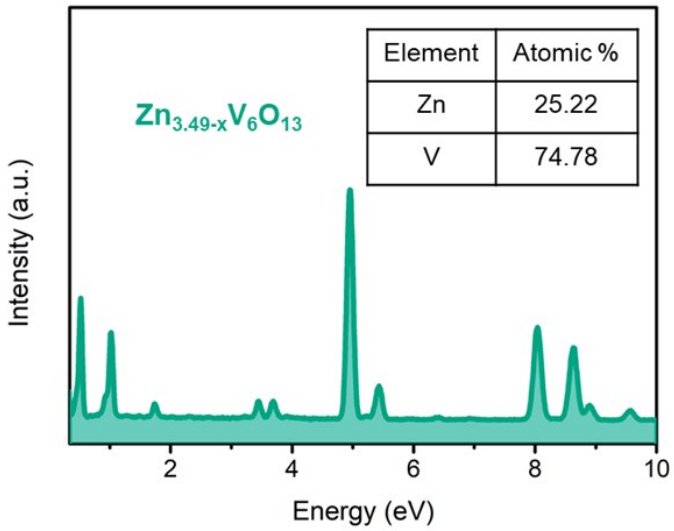

Figure S23. Transmission electron microscopy-energy dispersive spectrometer analysis of the air-recharged VCF and the quantification of elemental ratio.

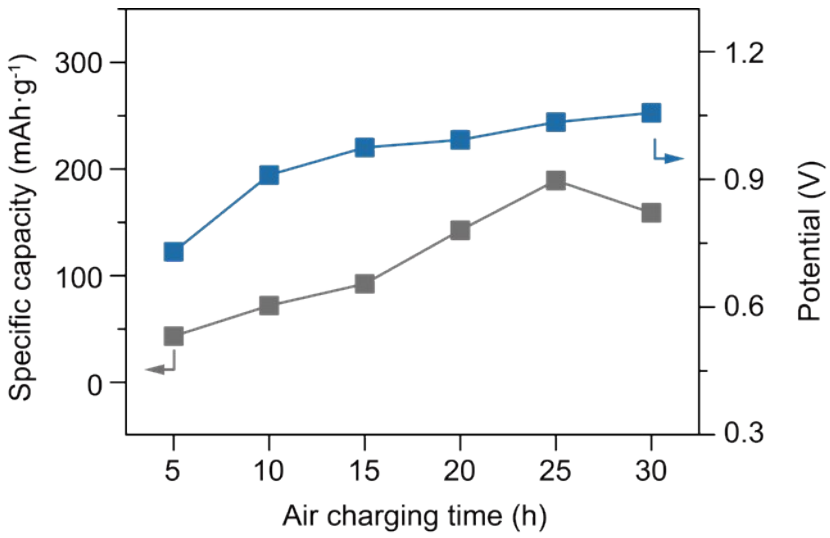

Figure S24. Effect of the air-recharging time on open-circuit voltage and discharge capacity of VCF/Zn battery fibers.

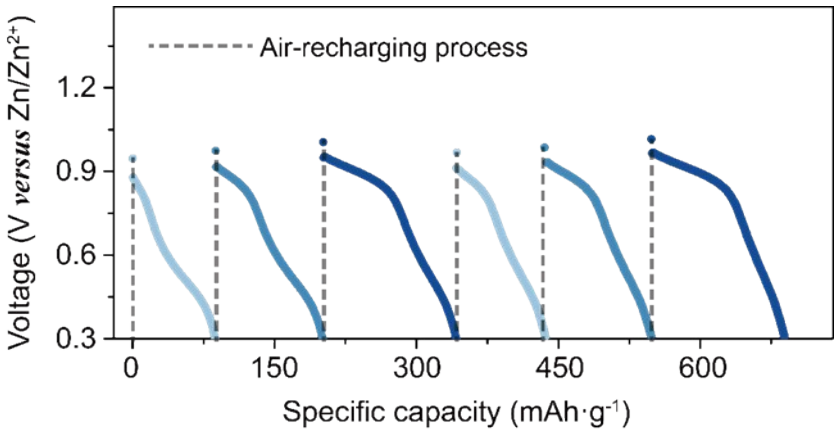

Figure S25. Voltage-time curves of the VCF/Zn battery fibers after being air-recharged to different states (dotted lines: air-recharging for different times. Solid lines: galvanostatic discharging at 100 $mA \cdot g^{-1}$).

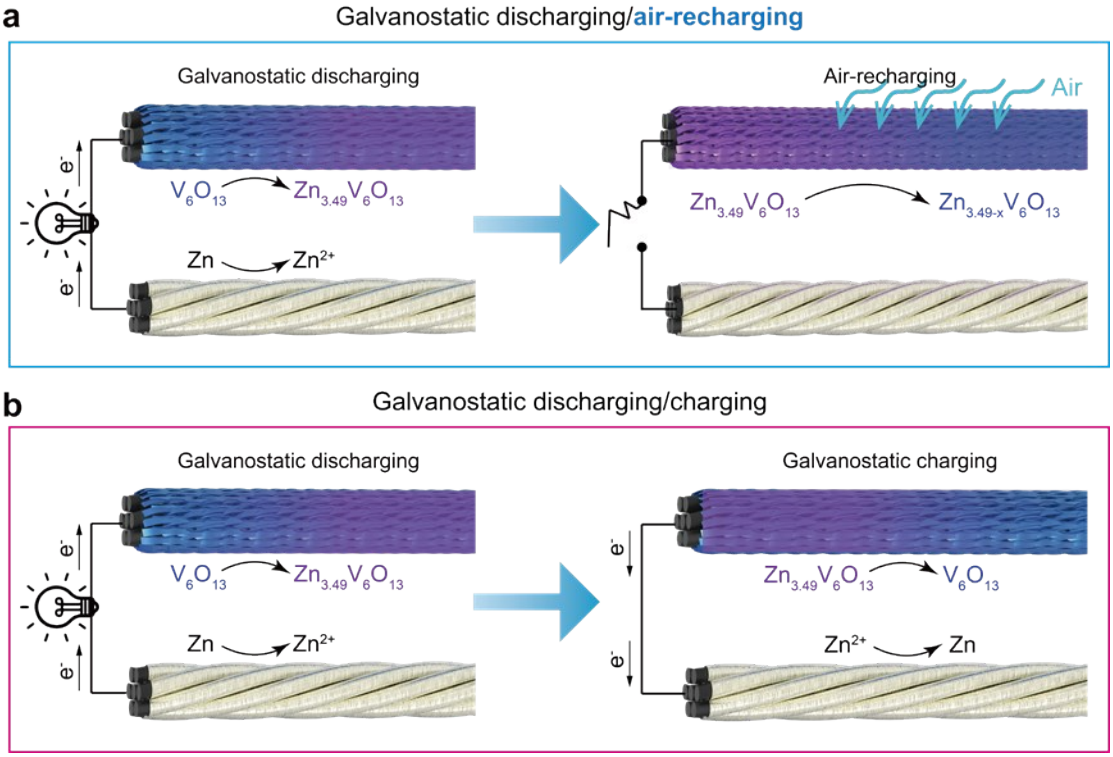

Figure S26. Schematic illustration of the galvanostatic discharging/air-recharging and the galvanostatic discharging/charging processes mentioned in **Figure 4d**.

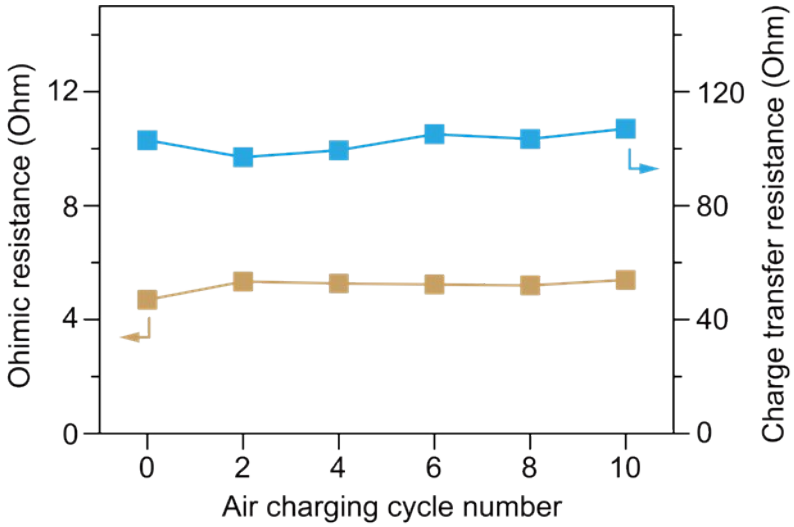

Figure S27. Ohmic resistances and charge transfer resistances recorded from different air-recharging cycles.

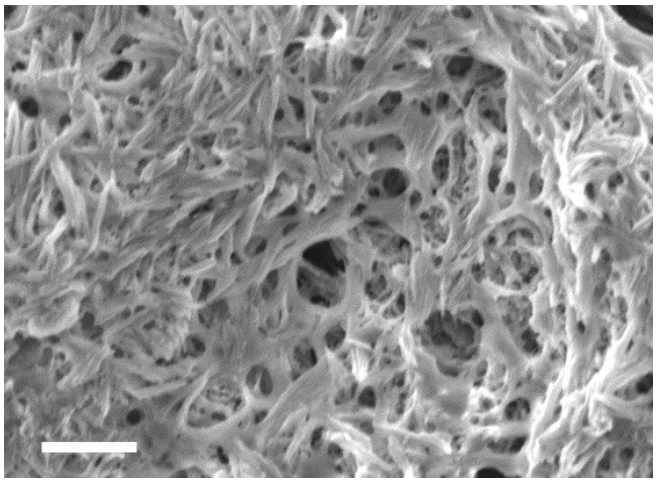

Figure S28. Surface morphology of the VCF after air-charging/galvanostatic discharging cycles. Scale bar, 200 nm.

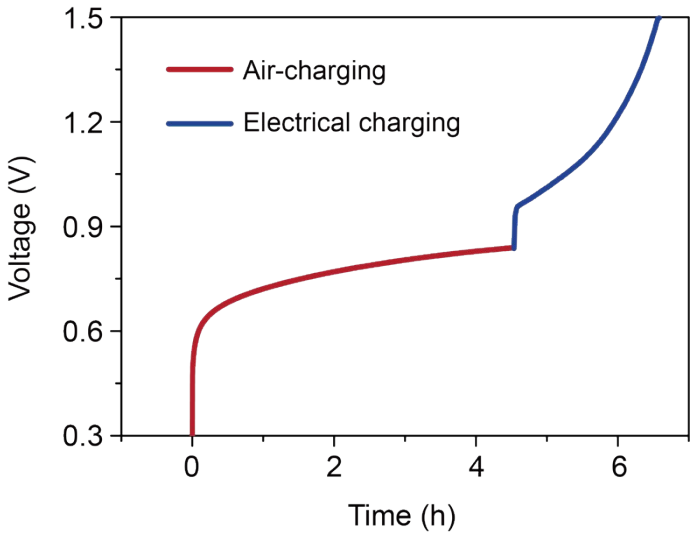

Figure S29. Charging behavior of the VCF/Zn battery fiber at the air charging/electrical charging hybrid mode.

Supporting Notes

1. Preparation of the multi-strand, aligned carbon nanotube fiber

Aligned carbon nanotube (CNT) fibers were continuously synthesized by previously reported floating catalyst chemical vapor deposition method and used as flexible current collectors in this work.[1] In a typical preparation, the composite catalyst of ferrocene (97%) and thiophene (3%) was first dispersed into the carbon source of ethanol (92%) and acetone (8%). The obtained solution was then bumped into a vertical reaction chamber (~1200-1300 ℃ of the heat reaction region inside the tuber furnace) controlled at a steady rate of 0.19 $mL \cdot min^{-1}$ by a peristaltic pump. A gas mixture of H_2 (1200 sccm) and Ar (200 sccm) was blown across the heat reaction region for chemical vapor deposition. The continuously formed CNT aerogels, synthesized from the above carbon source in a sock-like structure, was first soaked and condensed in a water coagulation bath. The as-obtained CNT aerogels were composed of CNT bundles with a typical bundle length of ~100 μm in a macroscopically aligned structure. Following that, the CNT aerogel was drawn through another water coagulation process for further contraction and drying procedure. The contracted CNT fibers were continuously collected by a rotator. 10-20 CNT fibers were further twisted to fabricate the multi-strand, aligned CNT fibers with diameter of ~200 μm as flexible current collectors without specific clarification.

2. Cyclic voltammetry (CV) study

The CV curves of the VCF/Zn fiber batteries at increasing scan rates from 0.1 to 1.0 $mV \cdot s^{-1}$ within a voltage window from 0.3 to 1.5 V were shown in **Figure S17**. Two pairs of redox peaks could be observed in CV curves. The relationship between obtained peak currents (***i***) and scan rates (***v***) was assumed to follow the equation as below

$$i = av^b,$$

which could also be presented as

$$\log(i) = blog(v) + log(a),$$

where *b* represented the slope of log(***i***) *versus* log(***v***) curve. Peak 1 and 2 labelled in **Figure S17** were selected as typical indicators for kinetics analysis of the VCF/Zn battery fiber. By fitting the plots of log(***i***) *versus* log(***v***), the *b* values of Peak 1 and 2 were calculated to be 0.861 and 0.835, respectively. The calculated *b* values were both in the range of 0 to 1, suggesting that the charge and discharge processes of the VCF/Zn battery fiber were controlled synchronously by ionic diffusion and pseudocapacitance. In addition, the capacitive contribution could be further determined by the equation as below

$$i = k_1 v + k_2 v^{\frac{1}{2}},$$

which could also be represented as

$$\frac{i}{v^{\frac{1}{2}}} = k_1 v^{\frac{1}{2}} + k_2,$$

where *i*, $k_1 v$, and $k_2 v^{1/2}$ represented the current response, capacitive, and ionic diffusion contribution, respectively. The k_1 value could be obtained by fitting the $i/v^{1/2}$ *versus* $v^{1/2}$ plots, the capacitive contribution in VCF/Zn fiber batteries was calculated to be 81.9% at 0.1 mV·s^{-1}. Upon the increasing scan rates, the percentages of capacitive contribution increased to 83.5%, 85.1%, 89.6% and 93.4% at scan rates of 0.2, 0.5, 0.8 and 1.0 mV·s^{-1}, respectively. The above results indicated that the VCF/Zn fiber batteries showed facilitated charge transfer kinetics.[2]

3. Electrode reaction mechanism

The galvanostatic charge-discharge reactions of the VCF/Zn battery fibers were first explored by X-ray photoelectron spectroscopy analysis. As shown in **Figure S4**, the pristine VCF showed a fitted V 2p spectrum with two spin-orbit doublets, characteristic

of V^{5+} (peaks at 517.5 eV and 525 eV) and V^{4+} (peaks at 516.3 eV and 523.6 eV), indicating a multi-valent nature of the VCF composed of V_6O_{13}. It was worth noting that the peak intensity of V^{5+} demonstrated to be higher than that of V^{4+}, and the intensity ratio of V^{5+}:V^{4+} was calculated to be >2. This was higher than that of the traditional V_6O_{13} material obtained through hydrothermal methods. The V^{5+} rich feature in synthesized VCF could be ascribed to the generation of the V^{5+}-contained functional groups on the electrode fiber surface during the synthesis process.[3] It also indicated an easy oxidation from V^{4+} to V^{5+} on the surface considering that the detection depth of the X-ray photoelectron spectroscopy was only a few nanometers.[4] The reversible Zn^{2+} storage/release in galvanostatic charge-discharge processes was further determined in the evolution of Zn 2p spectra as discussed in main text (**Figure 2e**). The inserted amount of Zn^{2+} ions in the discharging process could be quantified by the transmission electron microscopy-energy dispersive spectrometer analysis along with the electron transfer number upon the galvanostatic charge and discharge processes. The elemental analysis in **Figure S16** demonstrated that the molar ratio of Zn/V in VCF nanobelts increased from 0.143 to 0.583 after full discharge at a current density of 100 $mA \cdot g^{-1}$. Under such a condition, the charge product in the VCF was determined as $Zn_{0.86}V_6O_{13}$, and the corresponding discharge product was $Zn_{3.49}V_6O_{13}$. The galvanostatic charge-discharge reactions of the flexible aqueous VCF/Zn battery fiber could be formulated as below

$$\text{Cathode: } V_6O_{13} + 3.49Zn^{2+} + 6.98e^- \leftrightarrow Zn_{3.49}V_6O_{13}$$

$$\text{Anode: } 3.49Zn \leftrightarrow 3.49Zn^{2+} + 6.98e^-$$

The air-recharging reaction mainly involved the discharged (reduced) VCF (e.g., $Zn_{3.49}V_6O_{13}$) and the aqueous $Zn(CF_3SO_3)_2$ electrolyte with dissolved O_2. The spontaneous oxidation of the discharged VCF was driven by the redox potential difference. During the air-recharging process, the vanadium in discharged VCF was oxidized to higher-valence-state, and the inserted Zn^{2+} ions were extracted from the cathode material as revealed by a decreased *d*-spacing from *in-situ* X-ray diffraction

measurements (**Figure 4d**). With regard for the acid condition in 3 M $Zn(CF_3SO_3)_2$ electrolyte adopted for VCF/Zn batteries, the existence of H^+ ions would lead to the reduction of dissolved O_2 from ambient air to H_2O. In the meanwhile, the discharged VCF ($Zn_{3.49}V_6O_{13}$) would be oxidized by O_2 with the release of Zn^{2+} ions. And these extracted Zn^{2+} ions would further react with the generated OH^- as well as the electrolyte to form the zinc salt, i.e., $Zn_x(CF_3SO_3)_y(OH)_{y-x}$ on the surface of the cathode fiber. Note that $Zn_x(CF_3SO_3)_y(OH)_{y-x}$ could be decomposed upon the galvanostatic process.[5] This enabled reversibility of the air-recharging capability as a reliable, alternative power backup strategy. Note that the air-recharging reaction would not occur with the absence of O_2. When the fully discharged VCF/Zn battery was immersed in N_2-saturated aqueous $Zn(CF_3SO_3)_2$ electrolyte, where most of the O_2 was removed, there only existed a quick surge within several minutes of the electrode potential (**Figure S22**). This could be attributed to the concentration polarization on the surface of discharged VCF without involvement of capacity retention. In stark contrast, the air-recharging process demonstrated a much slower upslope of the open-circuit voltage (**Figure 3b**), indicating the sufficient oxidation of the discharged VCF. Based on above discussions, the reaction of the air-recharging process could be formulated as below

$$Zn_{3.49}V_6O_{13} + \frac{x}{2}O_2 + xH_2O + yZn(CF_3SO_3)_2 \rightarrow Zn_{3.49-x}V_6O_{13} + Zn_{x+y}(CF_3SO_3)_{2y}(OH)_{2x}$$

References for the Supporting Information

1. L. Ye, M. Liao, T. Zhao, H. Sun, Y. Zhao, X. Sun, B. Wang, H. Peng, *Angew. Chem. Int. Ed.* **2019**, 58, 17054-17060.

2. M. Yan, P. He, Y. Chen, S. Wang, Q. Wei, K. Zhao, X. Xu, Q. An, Y. Shuang, Y. Shao, K. T. Mueller, L. Mai, J. Liu, J. Yang, *Adv. Mater.* **2018**, 30, 1703725.

7. P. He, J. Liu, X. Zhao, Z. Ding, P. Gao, L. Fan, *J. Mater. Chem. A* **2020**, 8, 10370-10376.

4. Y. Ding, Y. Wen, C. Wu, P. Aken, J. Maier, Y. Yu, *Nano Lett.* **2015**, *15*, 1388-1394.

5. Y. Zhang, F. Wan, S. Huang, S. Wang, Z. Niu, J. Chen, *Nat. Commun.* **2020**, 11, 2199.